AAAS
Research
Volume 2020, Article ID 6213981, 12 pages
https://doi.org/10.34133/2020/6213981

Research Article

Mg-Based Micromotors with Motion Responsive to Dual Stimuli

Kang Xiong, Leilei Xu, Jinwei Lin, Fangzhi Mou, and Jianguo Guan

State Key Laboratory of Advanced Technology for Materials Synthesis and Processing, International School of Materials Science and Engineering, Wuhan University of Technology, Wuhan 430070, China

Correspondence should be addressed to Leilei Xu; xull@whut.edu.cn and Jianguo Guan; guanjg@whut.edu.cn

Received 11 April 2020; Accepted 24 June 2020; Published 4 August 2020

Mg-based micromotors have emerged as an extremely attractive artificial micro/nanodevice, but suffered from uncontrollable propulsion and limited motion lifetime, restricting the fulfillment of complex tasks. Here, we have demonstrated Mg-based micromotors composed of Mg microspheres asymmetrically coated with Pt and temperature-sensitive poly(N-isopropylacrylamide) (PNIPAM) hydrogel layers in sequence. They can implement different motion behaviors stemming from the driving mechanism transformation when encountering catalyzed substrates such as H_2O_2 and respond to both H_2O_2 concentration and temperature in aqueous environment. The as-constructed Mg-based micromotors are self-propelled by Pt-catalyzed H_2O_2 decomposition following the self-consuming Mg-H_2O reaction. In this case, they could further generate bilateral bubbles and thus demonstrate unique self-limitation motion like hovering when the phase transformation of PNIPAM is triggered by decreasing temperature or when the H_2O_2 concentration after permeating across the PNIPAM hydrogel layer is high enough to facilitate bubble nucleation. Our work for the first time provides a stimuli-induced "hovering" strategy for self-propelled micromotors, which endows Mg-based micromotors with an intelligent response to the surroundings besides the significant extension of their motion lifetime.

1. Introduction

Inspired by microorganisms in nature, artificial micromotors that propel themselves by converting diverse energies have been designed to perform complex tasks, such as cargo transport [1–3], advanced nanomanufacturing [4, 5], and environment remediation in microscopic environments [6–11]. Their motile behavior also further endows them great advantages as next-generation nanorobotics used for biomedicine [12, 13].

Mg-based micromotors, as a typical class of self-consuming artificial micromotors, not only could be powerfully driven by the Mg-H_2O reaction in physiological condition but also produce a byproduct of Mg^{2+} ions, an additional nutritional ingredient that benefits the human bodies [14, 15]. Additionally, the vast quantities of therapeutic hydrogen generated in the propulsion can further be used to eliminate excessive hydroxyl radicals which are harmful to living bodies [16]. They displayed superior compatibility for biological systems and have already been applied for drug delivery in the gastrointestinal tract of mice with enhanced therapeutic efficacies [17–22]. However, they generally suffer from poor motion controllability and relatively short motion lifetime stemming from the single driving reaction and self-consuming feature and cannot stop their movement unless the solid "fuel" Mg cores are almost consumed [23, 24]. To prolong the lifetime and improve the motion controllability of Mg-based micromotors, several strategies have so far been developed including tuning the opening size, controlling the pitting anions, and being functionalized with photocatalysts [21, 25], soft hydrogels [26], or biological materials [19, 25, 27, 28]. Yet they still face challenges in stimuli-responding propulsion and desirable "on/off" characteristics, and further efforts are necessary toward intelligence and controllability, which may lay the foundation for Mg-based micromotors to fulfill tasks in complex environments.

Here, we present a Mg-based micromotor with motion responsive to both H_2O_2 concentration and temperature in the surroundings. It consists of a Mg microsphere asymmetrically coated with Pt and temperature-sensitive poly(N-isopropylacrylamide) (PNIPAM) hydrogel layers in sequence. It can demonstrate the propulsion mechanism transformation between Mg-H_2O reaction and Pt-catalyzed H_2O_2 decomposition and unique concentration- or temperature-

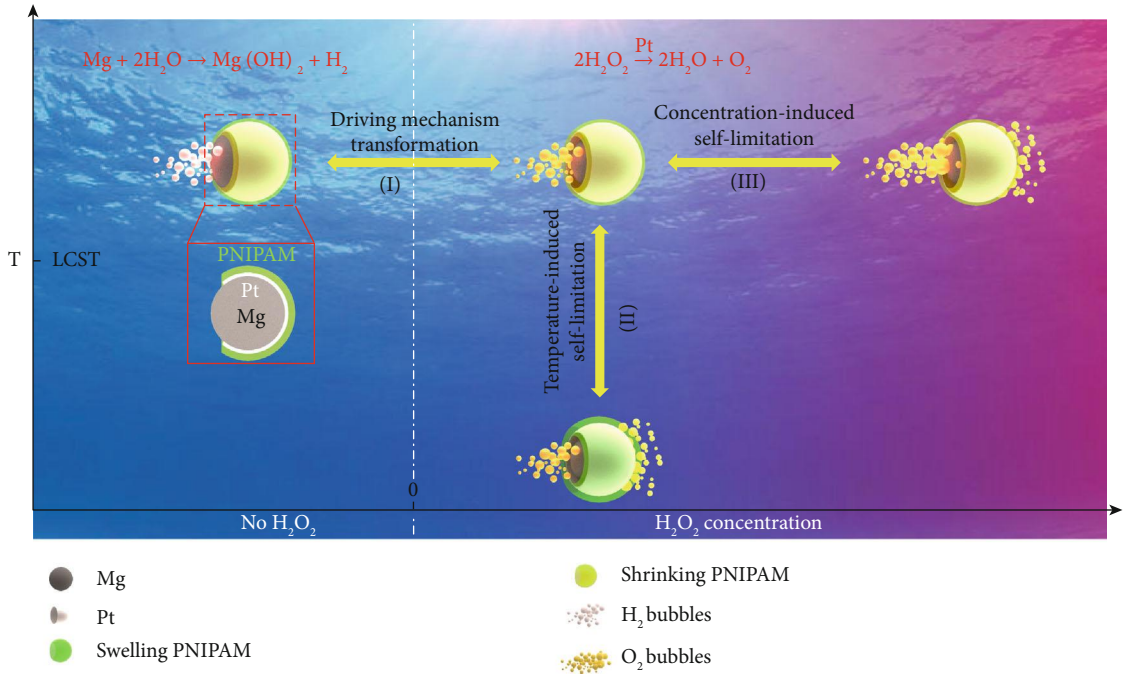

Figure 1: Schematic illustration of the Mg-based micromotor showing motion responsiveness to dual stimuli of temperature and H_2O_2 concentration. (I) The driving mechanism of the Mg-based micromotor is transformed from self-consuming Mg-H_2O reaction to Pt-catalyzed H_2O_2 decomposition once H_2O_2 appears in the solution. (II) Temperature-induced volume phase transformation of PNIPAM induces the transformation of motion behaviors. When temperature is lower than LCST, the covered PNIPAM hydrogel layer swells to increase the amount of permeated H_2O_2 and thus the catalytically generated oxygen on the side of the PNIPAM hydrogel layer, resulting in a self-limitation motion of the Mg-based micromotor like hovering due to bubble O_2 recoils from bilateral sides. (III) Concentration gradient of H_2O_2 induces the transformation of motion behaviors. Increasing H_2O_2 concentration raises the H_2O_2 concentration gradient between the two sides of the hydrogel layer, which facilitates H_2O_2 to cross the PNIPAM hydrogel layer and react with the middle Pt layer to form O_2 bubbles. Consequently, a self-limitation behavior of the Mg-based micromotor occurs due to bilateral O_2 bubble generation.

induced self-limitation behaviors like hovering. The temperature-induced volume phase transformation (swelling/shrinking) of PNIPAM and the H_2O_2 concentration both affect the permeability of H_2O_2 into the hydrogel layer and thus make the generation of O_2 bubbles in either single or bilateral sides, resulting in self-limitation motion. This work presents a stimuli-induced "hovering" strategy for the manipulation of Mg-based micromotors as well as a method for prolonging their lifetime by taking use of fuels from the surroundings. Given the possible changes of H_2O_2 concentration and temperature in human bodies, especially in diseased sites, the herein reported dual stimuli-responsiveness of Mg-based micromotors with extended motion lifetime may to some extent promise potential advanced biomedical applications.

2. Results and Discussion

Given the motion environment diversity of micromotors when used, we focus on the changes of chemical reaction propulsion mechanism and dual stimuli-responsive motion behaviors of Mg-based micromotors in the liquid environment system. The aim is to achieve their long-term lifetime and motion manipulation. In view of the popularity of temperature difference and low concentration H_2O_2 in either biological or environmental system, we have integrated Mg microspheres with catalytically active Pt to H_2O_2 and temperature-responsive poly(N-isopropylacrylamide) (PNIPAM) hydrogels to construct Mg-based micromotors. They were fabricated by asymmetrically coating Mg microspheres with Pt and PNIPAM hydrogel layers in sequence via magnetron sputtering and UV polymerization techniques according to our previous literature [29]. The as-fabricated Mg-based micromotors are about 40 μm in size and exhibit "opening" of about 14 μm of the surface (Figures S1 and S2). As shown in Figure 1, the Mg-based micromotor when operated in an aqueous solution (e.g., containing $NaHCO_3$ and poly(vinylpyrrolidone) (PVP)) is driven by asymmetrical H_2 bubble release generated by Mg-H_2O reaction due to the effective shielding of Pt layer from water in a gradually increasing confined space. When encountering catalyzed substrates such as H_2O_2, the propulsion mechanism of the Mg-based micromotor will transform spontaneously from the self-consuming Mg-H_2O reaction into Pt-catalyzed H_2O_2 decomposition. As H_2O_2 ($HO_2^- + H_2O + 2e^- \longrightarrow 3OH^-$, $E^0 = 0.878$ V vs. SHE) has a stronger oxidization ability than H_2O ($2H_2O + 2e^- \longrightarrow H_2 + 2OH^-$, $E^0 = -0.83$ V vs. SHE) [30], the reaction of Mg and H_2O_2 is much easier to occur than the Mg-H_2O reaction. As a result, O_2 bubbles from Pt-catalyzed H_2O_2 decomposition instead of H_2 bubbles propel the micromotor and the motion lifetime could be prolonged due to the transformation of driving reactions

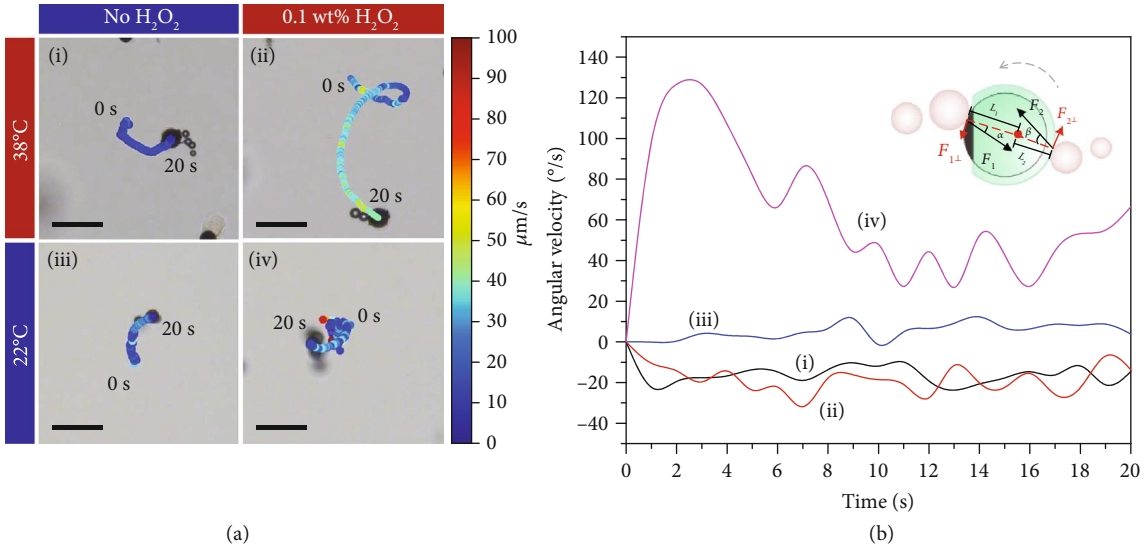

(a) (b)

FIGURE 2: The motion responsiveness of the as-prepared Mg-based micromotors to temperature and H_2O_2. (a) Time-lapse microscope images of the Mg-based micromotor moving in aqueous solutions. Scale bar: 100 μm. All systems contain 0.5 M $NaHCO_3$ and 5 wt% PVP, and the color of the trajectory points represents the instantaneous speed of the Mg-based micromotor. (b) The corresponding angular velocities of the Mg-based micromotor in the four motion states of (a). The clockwise is specified as the positive direction. The inset is the schematic of force analysis for the Mg-based micromotor. The bubble breaks out of the micromotor and gives it a recoil (F_1 and F_2) that contributes forces ($F_{1\perp}$ and $F_{2\perp}$) for the motor rotation and translational motion toward the opposite direction of bubble generation, respectively. α and β are the angles between the directions of the centroid connection line and $F_\perp$; L_1 and L_2 are the vertical distances between the center of mass of the Mg-based micromotor and $F_{1\perp}$ and $F_{2\perp}$.

from the self-consuming mode to the catalytic mode. When the temperature is below the lower critical solution temperature (LCST, 32°C), the PNIPAM hydrogel is in the hydrophilic swelling state and has a large diffusion constant to solution [31]. Consequently, H_2O_2 aqueous solution can easily penetrate the gel layer to react with the middle Pt layer resulting in a temperature-induced self-limitation motion like hovering due to bubble O_2 recoils from bilateral sides. Here, the self-limitation motion behavior means that a micromotor moves in 20 s only within a circle with the radius less than its twice size. The area of the motion region is characterized as $S_{20} = \pi\{(x_{Max} - x_0)^2 + (y_{Max} - y_0)^2\}$; here (x_{Max}, y_{Max}) is the farthest track point and (x_0, y_0) is the initial track point in 20 s. A similar transformation of motion behavior can also be triggered by increasing H_2O_2 concentration denoted as a concentration-induced self-limitation. A high concentration of H_2O_2 increases the concentration gradient between the two sides of the gel layer, inducing more H_2O_2 through the PNIPAM hydrogel layer for bilateral O_2 bubble generation. In a word, the as-constructed Mg-based micromotor can implement different motion behaviors stemming from the propulsion mechanism transformation when encountering Pt-catalyzed substrates such as H_2O_2 and respond to both the concentration of catalyzed substrates and temperature in aqueous environment with extended motion lifetime. This suggests that the as-prepared Mg-based micromotor may be taken as an example to address its intrinsic drawbacks of uncontrollable propulsion and limited motion lifetime arising from its self-consuming features. Although the H_2O_2 concentration used here is not in the nontoxic physiological range of less about 50 μM, the "fuel" concentration for the effective motor driving can be reduced via enhancing catalytic reaction activities, regulating motor structures, and so on [32, 33]. Moreover, the LCST of the hydrogel can be adjusted to fit the body temperature range by copolymerization [34, 35]. Thus, this will to some extent promote the development of Mg-based micromotors toward biomedical application.

Figure 2 and Video S1 show the motion behaviors of the Mg-based micromotor in the aqueous solution without or with 0.1 wt% H_2O_2 at 38°C or 22°C, respectively. All systems contain 0.5 M $NaHCO_3$ and 5 wt% PVP to peel off the $Mg(OH)_2$ passivation layer in Mg-H_2O reaction and to facilitate the suspension of the micromotor [36–38]. As shown in Figure 2(a), the Mg-based micromotor displays an obviously increased speed from 14.3 μm/s to 28.7 μm/s when moving from the aqueous solution without H_2O_2 (Figure 2(a), i) to that with 0.1 wt% H_2O_2 (Figure 2(a), ii) at 38°C. The speed increase is caused by evidently accelerating bubble formation and detachment, suggesting the possible driving mechanism transformation from Mg-H_2O reaction to Pt-catalyzed H_2O_2 decomposition. In the presence of H_2O_2, metal Mg prefers to react with H_2O_2 without H_2 production rather than with H_2O because of the higher reduction potential of H_2O_2 (0.878 V vs. SHE) than H_2O (-0.83 V vs. SHE) [30]. Simultaneously, Pt-catalyzed H_2O_2 decomposition has a much higher rate constant (about 3.60×10^{-2} min^{-1}) than Mg-H_2O reaction (about 1.05×10^{-2} min^{-1}) at an approximate pH of 7 [39, 40]. Additionally, the lower critical nucleation concentration of O_2 (68 mM) is much lower than that of H_2 (about 250 mM) bubbles [41, 42]. Both can induce vast quantities of O_2 bubble generation to powerfully drive the motor.

As the PNIPAM hydrogel is a temperature-responsive polymer with LCST, it usually exhibits a sharp volume phase transition at LCST, which is slowed by further increasing/decreasing temperature [43]. On the basis of the swelling-shrinking kinetics of the PNIPAM hydrogel, the collective diffusion coefficient for swelling ($D_0 = 2.0 \times 10^{-7}$ cm^2 s^{-1}) is about twice than that for shrinking ($D_0 = 1.1 \times 10^{-7}$ cm^2 s^{-1}) [44, 45]. Although at the temperature below the LCST (32°C) the PNIPAM has a volume swelling with a large cooperative (collective) diffusion of the gel network [31, 44], the micromotor can only be propelled by asymmetrical bubble recoils during the Mg-H_2O reaction because of the effective blocking from water by the middle Pt layer (Figure 2(a), i and iii). This will change when H_2O_2 appears in the system. As shown in Figure 2(a), iv, the micromotor shows an enhanced rotation with a decreased speed of about 15.8 μm/s and a decreased S_{20}, which looks like hovering because of bilateral bubble generation and release. This can be explained by the assumption that H_2O_2 aqueous solution may diffuse across the swelling hydrogel layer, reacting with the middle Pt layer to induce a self-limitation motion behavior of the Mg-based micromotor.

In order to explicate the temperature-induced self-limitation behavior, the corresponding angular velocity curves of Figure 2(a) are given in Figure 2(b). The single-side bubble-propelled micromotors (i, ii, and iii) show similar angular velocity curves with placid angular changes, while the bilateral-side bubble-propelled micromotor shows a relatively large angular change (iv). This can well explain the originality of the observed self-limitation state of the micromotor shown in Figure 2(a), iv. Under low Reynolds number conditions, the inertial effect can be neglected. The motion of the as-prepared Mg-based micromotor can be described by a set of differential equations for translation and rotation [46–48]:

$$\begin{aligned} m\frac{dv}{dt} &= F_{\text{Stokes}} + F_{\text{Brownian}} + F_{\text{drive}}, \\ J\frac{d\omega}{dt} &= T_{\text{Stokes}} + T_{\text{Brownian}} + T_{\text{drive}}, \end{aligned} \tag{1}$$

where m represents the mass of the motor, J is the inertia tensor, and v and ω denote the translation velocity and angular velocity. The terms that distinguish these Langevin equations from standard Langevin equations for inactive Brownian particles are the driving force and torque contributions arising from bubble detachment. Thereinto, F_{Brownian} and T_{Brownian} represent the diffusion arising from the Brownian force and torque with zero mean. The purely Brownian force for a passive particle can be described by a theoretical translational diffusion coefficient ($D_T = k_B T/6\pi\eta R$) [49] and a rotational diffusion coefficient ($\tau_R^{-1} = k_B T/8\pi\eta R^3$) [50]. In this system, as a spherical particle with a radius about 40 μm, the characteristic time scale for rotational diffusion τ_R and translational diffusion coefficient D_T is calculated to be 728.5 min and 1.22×10^{-10} cm^2/s, respectively. This means the effect of Brownian force on the motion of the as-prepared micromotor is limited. F_{drive} and T_{drive} are the reaction force and torque caused by the detachment of the bubbles, which will be balanced by the Stokes viscous drag force generated in the opposite direction during motion. Because of the spherical structure of the as-prepared micromotor, $F_{\text{Stokes}} = 6\pi\eta Rv$ (for translation) and $T_{\text{Stokes}} = 8\pi\eta R^3\omega$, where R is the particle (hydrodynamic) radius and η is the fluid viscosity. For the motion of the as-prepared Mg-based micromotor, the contributions of F_{Stokes} and T_{Stokes} are passive depending on v and ω and the rotation of bubble recoil-propelled micromotors mainly arises from the bubble detachment deviating from their symmetry [26, 51–53]. Therefore, a simplified force analysis of a micromotor based on the driving force is used to understand the motion states. F_1 and F_2 represent the instant propulsion forces provided by the bubble detachment from the opening and the coated side, respectively. For the cases shown in Figure 2(a), i, ii, and iii, $F_2 = 0$ and the micromotor is only driven by single-side bubble recoil on the opening. Their rotational motions are all caused by the rotational component of F_1 contributing an instant torque expressed as $T_1 = F_{1\perp}L_1 = F_1L_1 \sin\alpha$, where $F_{1\perp}$ represents the vertical component of F_1 for motor rotation, L_1 is the effective lever arm, and α is the angle between the directions of the centroid connection line and $F_{1\perp}$. The differences in their motion states including translational and rotational velocities as well as rotational directions mainly depend on α and the bubble detachment positions. For the micromotor moving in 0.1 wt% H_2O_2 aqueous solution at 22°C, neither F_1 nor F_2 is 0 due to bilateral bubble generation and ejection. As a result, the instantaneous torque that contributed to the micromotor's rotation is the vector sum of the two torques: T_1 ($T_1 = F_1L_1 \sin\alpha$) generated by bubble escape from the open end and T_2 ($T_2 = F_2L_2 \sin\beta$) generated by bubble release from the coating side. When $\alpha\beta > 0$, the micromotor exhibits an enhanced rotation corresponding to a large angular velocity (Figure 2(b), iv), while it shows a weakened rotation as $\alpha\beta < 0$ (Figure S3, Video S2). The self-limitation behavior of the Mg-based micromotor in the H_2O_2 aqueous solution below the LCST of PNIPAM is attributed to the enhanced rotation caused by the bilateral-side bubble detachments.

The dissolved H_2 and O_2 in the aqueous solution before and after adding H_2O_2 are determined to verify the driving mechanism transformation from the self-consuming Mg-H_2O reaction to the Pt-catalyzed H_2O_2 decomposition. Figure 3 shows that when the motors move in the aqueous solution without H_2O_2, the dissolved H_2 in the solution increases gradually. This indicates that the driving reaction at this moment is a H_2-produced reaction as $Mg + H_2O + 2HCO_3^- \rightleftharpoons MgCO_3 + CO_3^{2-} + 2H_2$. When H_2O_2 is introduced into the solution at 301 s, the dissolved H_2 drops sharply, while the dissolved O_2 rises from 2.7 mg/L to 19.9 mg/L. This implies that the driving reaction of the Mg-based micromotors is transformed to Pt-catalyzed H_2O_2 decomposition (producing O_2) instead of the Mg-H_2O reaction (producing H_2). The initial O_2 concentration in the aqueous solution stems from dissolved air. This transformation arises from the strong oxidization of H_2O_2 with a much higher electrode potential than that of H_2O [30]. In the

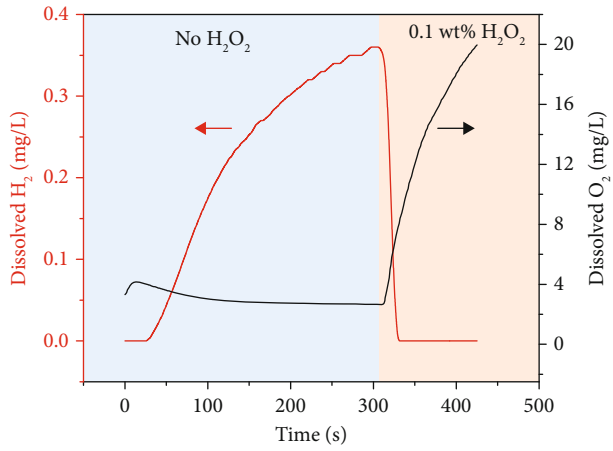

FIGURE 3: The diagram of dissolved H_2 and O_2 over time before and after adding H_2O_2 in the motion system containing 0.5 M $NaHCO_3$ and 5 wt% PVP.

presence of H_2O_2, Mg prefers to react with H_2O_2 without generating H_2 rather than to react with H_2O [54] and simultaneously Pt-catalyzed H_2O_2 decomposition can produce O_2 gas. This can be further verified by the fact that no bubble generates when bare Mg microparticles are put in H_2O_2 aqueous solution (Video S3).

As discussed above, the Mg-based micromotor can be driven by both Mg-H_2O reaction in the aqueous solution without H_2O_2 and Pt-catalyzed H_2O_2 decomposition when meeting H_2O_2. In the aqueous solution containing $NaHCO_3$ and PVP but without H_2O_2, the Mg core is consumed continuously via the Mg-H_2O reaction to produce numerous H_2 bubbles that propel the micromotor due to the conservation of momentum [55]. Figure 4 shows the Mg core amounts and motion speeds versus time, respectively. After overcoming the initial gravity-induced subsidence (Figure S4 and Video S4), the micromotor keeps moving by bubble recoils with the Mg core amount continuously decreasing as shown in Figure 4(a) and Video S5, indicating its self-consumed feature. At this time, the lifetime of the micromotor mainly depends on the opening size (Figure S5) and is in the range of a few minutes to dozens of minutes. With the Mg-H_2O reaction proceeding, there forms a confined space inside the micromotor, where the nucleation and growth of H_2 bubbles occur. At the early stages, the ejected bubbles are small, while they become large when the Mg core is almost gone. The size of the formed bubbles is mainly dependent on the growth time in the confined space. At the initial stages, the narrow space between the Mg core and the coating layer is too narrow for the growth of bubbles before they eject from the micromotor due to the capillary effect. Upon the enlarged confined space over time, the growth period is extended resulting in the formation of large bubbles. Figure 4(b) shows that the as-prepared micromotor has a relatively constant motion speed and consumption rate of the Mg core during Mg-H_2O reaction. This is not in agreement with the previous reported surface area-related reaction rate and can be explained by the effect of the confined space, in which the permeation of water is competitive with the escape of bubbles.

The as-constructed Mg-based micromotors can improve the motion controllability and lifetime by the spontaneous transformation of propulsion mechanisms from the self-consuming reaction to the catalytic reaction in terms of the surroundings. In H_2O_2 aqueous solution, the as-prepared Mg-based micromotor can be driven by Pt-catalyzed H_2O_2 decomposition and keeps constantly moving until the fuel (H_2O_2) runs out. The lifetime of the motor moving in H_2O_2 aqueous solution is determined by the amount of H_2O_2 and has been significantly prolonged because of the far excess "fuel" in the system. Figure 5 shows the effect of H_2O_2 concentration on the motion behaviors of the Mg-based micromotors. Taking a micromotor moving at 38°C for example, the as-prepared micromotor first accelerates and then decelerates the motion with increasing the H_2O_2 concentration (Figure 5(a)). This is dramatically different from the previously reported catalytic micromotors, whose speeds generally increase with increasing catalytic substrate concentrations [56–58]. The speeds of the Mg-based micromotor before and after the addition of H_2O_2 with different concentrations are shown in Figure S6. When the micromotor moves in the solution without H_2O_2, the motion speed is basically stable with an average value of about 13.2 μm/s depending on the relatively constant H_2 bubble size and generation frequency (Video S5). After adding H_2O_2, the motion speeds of the micromotor contributed by O_2 detachment from Pt-catalyzed H_2O_2 decomposition are closely related to H_2O_2 concentration. The initial increase of the speed with increasing H_2O_2 concentration (0~0.4 wt%) is attributed to an increased bubble generation frequency. The large variability of speed in 0.4 wt% H_2O_2 aqueous solution may be attributed to the rapid changes of α and the bubble escape positions in motion (Video S6). The remarkable decrease of motion speed occurs as the H_2O_2 concentration is further increased to 0.8 wt%, implying a possible change of motion behavior. As shown in Figure 5(b) and Video S7, the micromotor displays a self-limitation motion like hovering due to the bilateral O_2 bubble generation and release as H_2O_2 concentration is higher than 0.8 wt%. This indirectly reduces the asymmetry of the micromotor and leads to the reduction of the speed. After diluting 0.8 wt% H_2O_2 aqueous solution to 0.67 wt%, the micromotor shows a curved ballistic trajectory as the O_2 bubbles are released from the opening instead of bilateral release, while the bilateral O_2 bubble generation and detachment occur again after supplementing H_2O_2 to 1.23 wt%. In other words, the as-prepared micromotor exhibits a self-limitation behavior in a relatively high-concentration H_2O_2 aqueous solution and returns to a curved ballistic motion at a low concentration. The transformation is reversible with changing the concentration of H_2O_2. Such unique concentration-induced self-limitation is associated with the permeability of H_2O_2 into the PNIPAM hydrogel layer. A high concentration of H_2O_2 aqueous solution can form a large concentration gradient between the two sides of the hydrogel layer to facilitate more H_2O_2 across the

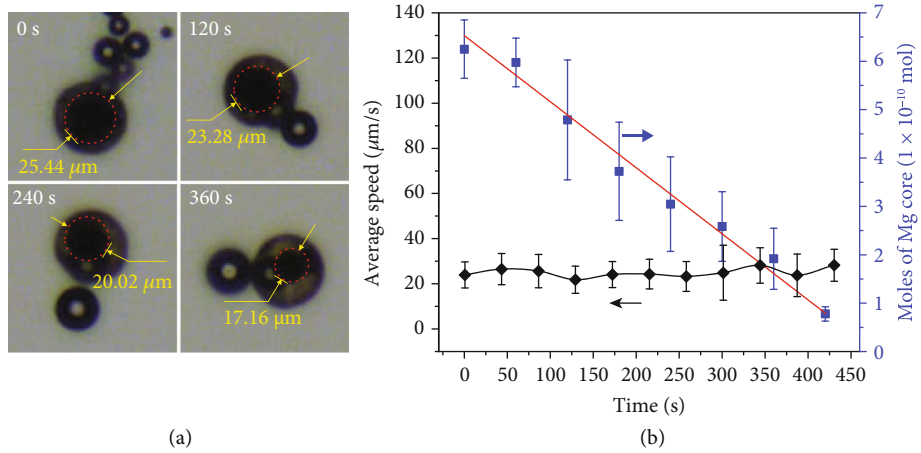

Figure 4: The Mg-based micromotor propelled by the Mg-H_2O reaction. (a) Time-lapse microscope images of Mg core consumption in the solution without H_2O_2. (b) The corresponding average speeds in every 40 s of the Mg-based micromotor and Mg core amounts versus time. The red line indicates the fitting line for Mg core consumption.

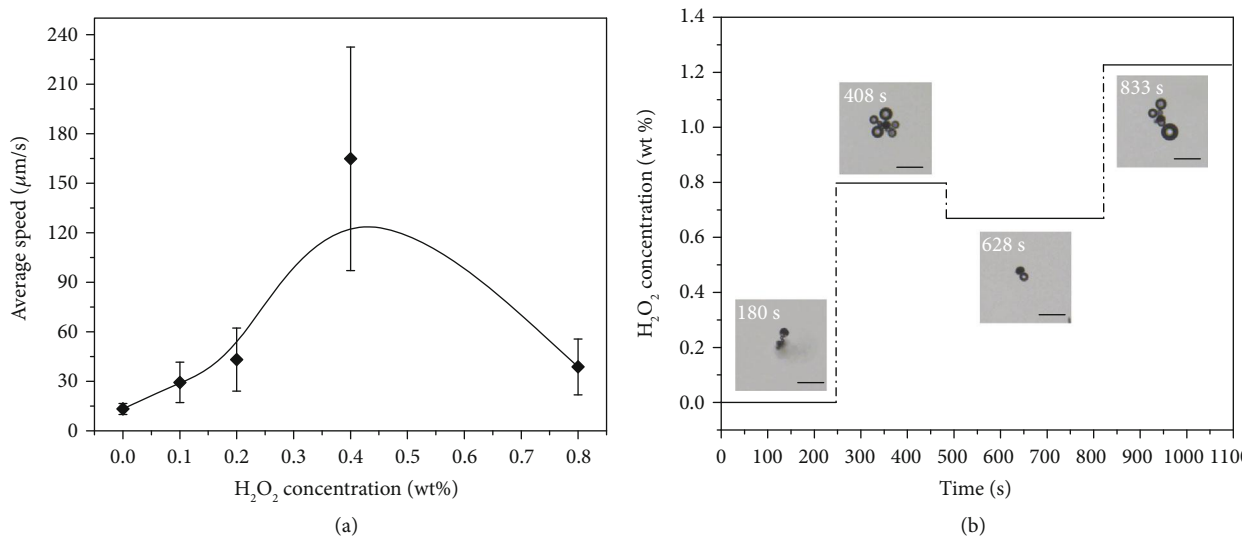

Figure 5: The effect of H_2O_2 concentration on motion behaviors of the Mg-based micromotor. (a) The average speed of the Mg-based micromotor in a solution with different concentrations of H_2O_2 at 38°C. The black line represents the trend line. (b) The H_2O_2 concentration of the aqueous solution containing the Mg-based micromotor versus time. The insets show typical states of the micromotor in each period, and the dotted line represents a transitional period after which a constant local H_2O_2 concentration is available in the system. Scale bar: 100 μm. In the aqueous solution without H_2O_2 (0~250 s), bubbles generate from the open end of the Mg-based micromotor, while adding H_2O_2 to raise the concentration to 0.8 wt% results in bilateral bubble production (250~480 s). Further reducing H_2O_2 concentration to 0.67 wt% via diluting makes the reaction occur in a unilateral side (480~820 s), and the reaction again occurs in bilateral sides when the concentration reaches 1.23 wt% by adding H_2O_2 again (820~1100 s).

PNIPAM hydrogel layer and react with the middle Pt layer. As a result, the generated O_2 accumulates and reaches the heterogeneous nucleation energy on the side of the hydrogel layer for O_2 bubble nucleation and growth, resulting in a concentration-induced self-limitation.

To further illustrate the temperature/concentration-dependent self-limitation motion mechanisms of the Mg-based micromotor driven by Pt-catalyzed H_2O_2 decomposition, we have carried out numerical simulations over the Mg-based micromotor based on a 2D model (Figure S7) by chemical reaction engineering and dilute chemical species transport modules of COMSOL Multiphysics. Figure 6 shows the numerical simulation results of O_2 concentration distribution around the Mg-based micromotor with different temperatures and H_2O_2 concentrations. It should be noted that the simplified model only considers the O_2 concentration distribution for nucleation and ignores the fluid disturbance deriving from micromotor motion. In this model, the PNIPAM coating is treated as a porous media, because the swelling/shrinking of the hydrogel network can result in different porosities for O_2 diffusion, which is temperature-dependent. In a swelling state, a large cooperative diffusion coefficient benefits the permeation of H_2O_2 through the hydrogel layer resulting in a network

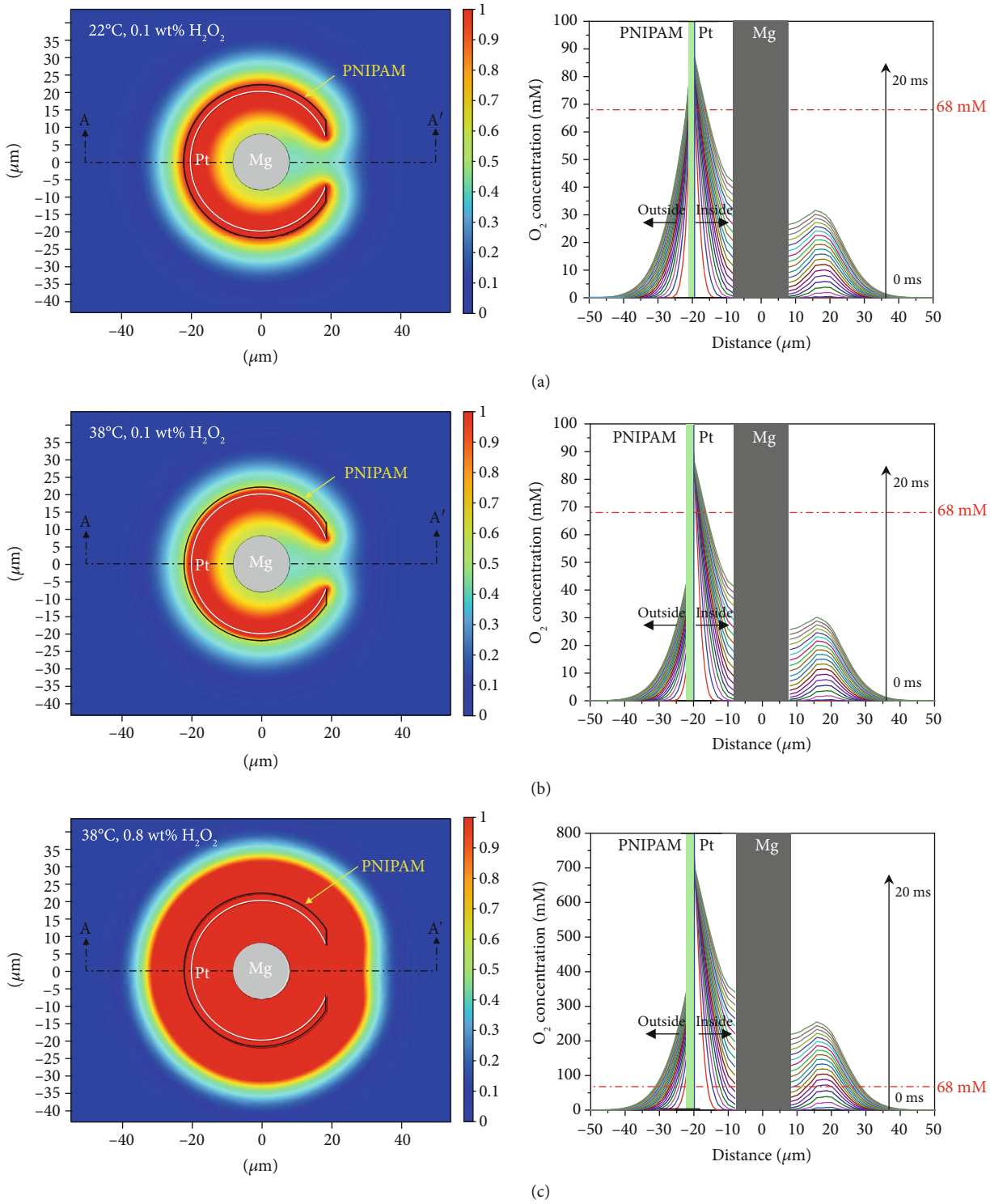

FIGURE 6: The normalized O_2 concentration distribution around the Mg-based micromotor at (a) 22°C in 0.1 wt% H_2O_2, (b) 38°C in 0.1 wt% H_2O_2, and (c) 38°C in 0.8 wt% H_2O_2 aqueous solution. The right panels show the curves of theoretical O_2 concentration on AA′ line segments within 20 ms versus the distance apart from the center of Mg core at different time intervals. The critical nucleation concentration of O_2 bubble is 68 mM.

with large porosity, which is approximately twice than that in a shrinking state [44, 59]. When the micromotor is moving below the LCST at a low-concentration H_2O_2 aqueous solution of 0.1 wt%, the O_2 generated inside the coating layer will reach the critical nucleation concentration of 68 mM within 1 ms due to the accumulative effect of the inner confined void (Figure 6(a)). Simultaneously, in view of the water-swelling feature of the PNIPAM hydrogel layer at

this temperature, there are more H_2O_2 permeating across the hydrogel layer to react with the middle Pt layer resulting in O_2 nucleation on the side of the hydrogel layer. As a result, the micromotor shows a self-limitation behavior caused by bilateral O_2 bubble generation (Figure 2(a), iv). In contrast, by increasing temperature to 38°C, the access of H_2O_2 is slowed down by the contracted PNIPAM hydrogel layer. Consequently, the concentration of O_2 generated on the side of the hydrogel layer cannot reach its critical nucleation concentration under continuous outward diffusion (Figure 6(b)). Therefore, the inside generated O_2 bubble detachment from the opening is the origin of the sufficient propulsion of the as-prepared Mg-based micromotor (Figure 2(a), ii). However, increasing the H_2O_2 concentration to 0.8 wt% could facilitate the permeation of H_2O_2 aqueous solution into the PNIPAM hydrogel layer and the catalytic decomposition of H_2O_2 at the middle layer Pt (Figure 6(a)). This enables the O_2 generation on both sides of the middle Pt layer to reach the critical nucleation concentrations and thus induce self-limitation motion of the micromotor.

3. Conclusion

In this work, we present a kind of dual mechanism-propelled Mg-based micromotor with motion responsive to both temperature and H_2O_2 concentration. The as-constructed Mg-based micromotors are obtained by asymmetrically coating of Mg microspheres with catalytically active Pt and temperature-sensitive PNIPAM hydrogel layers in sequence. They can be propelled by Mg-H_2O reactions followed by Pt-catalyzed H_2O_2 decomposition when encountering H_2O_2 and exhibit extended motion lifetime. In the latter case, they would respond to both H_2O_2 concentration and temperature in solution environment, demonstrating unique temperature- and/or concentration-induced self-limitation motion like hovering. This is associated with the temperature-dependent diffusion coefficient and the concentration-related permeability of H_2O_2 aqueous solution in the PNIPAM hydrogel layer. Our results have for the first time demonstrated the Mg-based micromotors with motion responsive to external stimuli in a multifuel system and provided a strategy to push forward the development of intelligent Mg-based micromotors and to prolong the motion lifetime.

4. Materials and Methods

4.1. Materials. All the chemicals used in this work were of analytical grade and were used as received without further purification. Poly(vinylpyrrolidone) (PVP, K30), ethylene glycol (EG), hydrogen peroxide, N-isopropylacrylamide (NIPAM), bis(N,N-methylene bis(acrylamide)), 2,2-diethoxyacetophenone (DEAP), sodium bicarbonate ($NaHCO_3$), acetone, and ethanol were purchased from TCI (Shanghai) Development Co., Ltd., China. Commercial Mg microspheres were purchased from TangShan WeiHao Magnesium Powder Co. (Tangshan, China) and washed with acetone twice before usage.

4.2. Fabrication of the Mg-Based Micromotors. The Mg-based micromotors are prepared by our previously reported method with some modifications [29] shown in Figure S1. In detail, Mg microspheres with an average size of about 40 μm were completely scattered on the surface of a glass slide precoated with a thin poly(vinylpyrrolidone) (PVP, K30) film by dripping 100 μL 0.5 wt% PVP ethanol solution on the glass slide and then drying at 60°C for 10 min. Then, the PVP-glass slide with dispersed Mg microspheres was placed in humid air with a relative humidity of 50% for 20 s. During this process, Mg microspheres were partially immersed in the PVP film under the gravitational field to obtain partially covered carriers. After drying in an oven at 60°C for 10 min, the Mg microspheres with partially covered bottom surface were fixed in the PVP film. Then, the exposed Mg surfaces were coated with a Pt layer via magnetron sputtering for 240 s to obtain the Mg/Pt microspheres fixed. The poly(N-isopropylacrylamide) (PNIPAM) precursor solution was prepared by dissolving 0.35 g NIPAM in 3.5 mL EG followed by adding 0.2 g bis(N,N-methylene bis(acrylamide)) and 20 μL 2,2-DEAP into the solution. Subsequently, 100 μL PNIPAM-EG precursor solution was dropped onto the obtained glass slide to form a liquid film on the surface of the Mg/Pt microspheres fixed on the PVP-glass slide followed by spin-coating by a spin coater (speed of 2000 rpm, coating time of 50 s, EZ4 spin coater, Schwan Technology) and then covered by a slip. The obtained glass slide was exposed to the UV light to polymerize NIPAM for 240 s followed with removing the thin cover slips and drying in vacuum at 60°C for 12 h. Finally, the Mg-based micromotors were separated from the substrate by a blade-scratching process and washed with acetone twice to remove the PVP layer.

4.3. Motion Tests of the Mg-Based Micromotors. The movement of the as-prepared Mg-based micromotors was performed in 0.5 M $NaHCO_3$ aqueous solution with 5 wt% PVP as surfactant. In each test, 90 μL 0.5 M $NaHCO_3$ and 5 wt% PVP containing the micromotors were dispersed on a glass slide. The glass slide was heated from room temperature to the desired temperature using the microscope temperature control stage. Then, 10 μL H_2O_2 aqueous solution with different concentrations was dropped on the glass slide for observation and recorded with an optical microscope using a high-resolution CCD digital camera (Leica DM 3000B, Inc. Germany).

4.4. Determination of Dissolved H_2 and O_2. To measure dissolved O_2 and dissolved H_2 in the system, 20 mg Mg-based micromotors was added into 90 mL 0.5 M $NaHCO_3$ and 5 wt% PVP solution at 22°C. After 301 s, 10 mL 1 wt% H_2O_2 was added into the system. During the whole process, the data was measured and recorded by the portable dissolved H_2 and O_2 analyzers.

4.5. Characterizations. Scanning electron microscopy (SEM) images were taken with a Hitachi S-4800 (Japan) at an acceleration voltage of 10.0 kV. The energy dispersive spectroscopy (EDS) analyses were carried out on a JEOL

JEM-7500F (Tokyo, Japan) operated at an accelerating voltage of 15 kV. Magnetron Sputtering System (JCP500, Beijing Technol Science Co., Ltd., China) was used to cover the middle Pt layer. The microscopy images and the motion videos of micromotors were recorded with optical microscope using a high-resolution CCD digital camera (Leica DM 3000B, Inc. Germany) coupled with ×5, ×10, ×20, and ×40 objective. The temperature was heated by heating accessories (Temp-Controller 2000-1, Inc. Germany) of the microscope. All videos were analyzed by Video Spot Tracker V08.01 and Matlab R2018a software.

4.6. Numerical Simulation. In order to further confirm the role of temperature and H_2O_2 concentration in the transformation of the limitation behavior, a two-dimensional numerical simulation of the process is performed using a commercial COMSOL finite element analysis software. The chemical reaction engineering and dilute chemical species transport module are employed. Porous media transfer is used based on the effect of temperature on the PNIPAM hydrogel to simulate the response. The two-dimensional model is created according to the state of the motor at 360 s in Figure 4(a) with an approximately 50 nm Pt layer and 2 μm PNIPAM layer as shown in Figure S7. The reaction engineering module assumes a batch type reactor process with constant volume. The decomposition reaction is

$$2H_2O_2 \longrightarrow^{Pt} 2H_2O + O_2\uparrow \tag{2}$$

The reaction rate constant k_f changing with temperature according to Arrhenius expression is

$$k_f = A_f * \exp\left(\frac{-E_a}{RT}\right). \tag{3}$$

The values for activation energy E_a are given as 40 kJ/mol, frequency factor of collision A_f as 4.32×10^5 min^{-1}, and reaction rate constant k_f as 3.60×10^{-2} min^{-1} (for 22°C) and 8.32×10^{-2} min^{-1} (for 38°C). The surface species (catalyst) is kept with locked concentration. The governing equations in reaction engineering are

$$\frac{dc_i}{dt} = R_i + R_{\text{ads},i}\frac{A_r}{V_r}. \tag{4}$$

Here, for a species i, c_i is the concentration, R_i is the rate of the species, $R_{\text{ads},i}$ is the rate effect of surface species on i, A_r is the surface reaction area, and V_r is the reactor volume. The study is carried out with time steps of 1 to 20 ms. Transport of diluted species is used to compute the concentration field. The governing physics involves the use of Fick's law for transport by diffusion and adsorption as the adsorption happens on the catalytic surface. The products are formed when they are desorbed from the catalyst surface. And simplify the PNIPAM hydrogel into a porous medium. The governing equation for this problem is the conservative form of the transport of diluted species in porous media interface:

$$\begin{aligned} \frac{d(\varepsilon_p c_i)}{dt} + \nabla \bullet \mathbf{J}_i &= R_i, \\ \mathbf{J}_i &= -D_{e,i}\nabla c_i, \\ D_{e,i} &= \frac{\varepsilon_p}{\tau_{F,i}} D_{F,i}. \end{aligned} \tag{5}$$

Here, for a species i, $\mathbf{J}_i$ is the flux of the species, ε_p is the porosity of the hydrogel, $\tau_{F,i}$ is the tortuosity factor based on the Millington-Quirk model [60], $D_{F,i}$ is the diffusion coefficient of the species in fluid, and $D_{e,i}$ is the effective diffusion coefficient of the species. The typical simulation parameters are shown in Table S1.

Conflicts of Interest

The authors declare no competing financial interest.

Authors' Contributions

L. Xu and J. Guan conceived the idea and designed the experiments. K. Xiong and J. Lin performed the experiments. F. Mou gave suggestions about the experiments. K. Xiong performed the simulations. K. Xiong, L. Xu, and J. Guan analyzed the data and cowrote the manuscript. L. Xu and J. Guan initiated and supervised the study. All authors contributed to the discussion and gave approval to the final version of the manuscript.

Acknowledgments

his work was financially supported by the National Natural Science Foundation of China (21975195, 51521001, 21875175, and 21705123), the Fundamental Research Funds for the Central Universities (WUT: 2017III028 and 2018III012), and the Innovation and Entrepreneurship Training Program for National College Students of Wuhan University of Technology (201910497029).

Supplementary Materials

Supplementary 1. Figure S1: fabrication process of the Mg-based micromotors. Figure S2: SEM and EDS mapping images of a typical Mg-based micromotor. Figure S3: time-lapse microscope images of a typical Mg-based micromotor showing self-limitation with a small angular velocity (3.02°/s). Figure S4: initial gravity-induced subsidence of a typical Mg-based micromotor. Figure S5: the curve of the lifetime of a typical Mg-based micromotor versus the average opening size. Figure S6: instantaneous speed of the Mg-based micromotor before and after adding H_2O_2 with different concentrations. Figure S7: schematic of the two-dimensional model for the Mg-based micromotor. Table S1: typical parameters used in the simulations.

Supplementary 2. Supporting Video S1: a typical Mg-based micromotor moving without H_2O_2 (i and iii) or with 0.1 wt% H_2O_2 aqueous solution (ii and iv) at 38°C (i and ii) or 22°C (iii and iv), respectively.

Supplementary 3. Supporting Video S2: a typical Mg-based micromotor showing self-limitation with a small angular velocity (3.02°/s).

Supplementary 4. Supporting Video S3: the states of a typical bare Mg microparticle in the aqueous solution with or without H_2O_2.

Supplementary 5. Supporting Video S4: initial gravity-induced subsidence of a typical Mg-based micromotor.

Supplementary 6. Supporting Video S5: Mg core consumption during the Mg-H_2O reaction.

Supplementary 7. Supporting Video S6: a typical Mg-based micromotor moving in 0.4 wt% H_2O_2 aqueous solution.

Supplementary 8. Supporting Video S7: H_2O_2 concentration-dependent motion behaviors of a typical Mg-based micromotor.

References

[1] S. Tottori, L. Zhang, F. Qiu, K. K. Krawczyk, A. Franco-Obregón, and B. J. Nelson, "Magnetic Helical Micromachines: Fabrication, Controlled Swimming, and Cargo Transport," *Advanced Materials*, vol. 24, no. 6, pp. 811–816, 2012.

[2] K. Villa, F. Novotný, J. Zelenka, M. P. Browne, T. Ruml, and M. Pumera, "Visible-light-driven single-component $BiVO_4$ Micromotors with the autonomous ability for capturing microorganisms," *ACS Nano*, vol. 13, no. 7, pp. 8135–8145, 2019.

[3] T. Yang, T. O. Tasci, K. B. Neeves, N. Wu, and D. W. M. Marr, "Magnetic microlassos for reversible cargo capture, transport, and release," *Langmuir*, vol. 33, no. 23, pp. 5932–5937, 2017.

[4] J. Li, W. Gao, R. Dong, A. Pei, S. Sattayasamitsathit, and J. Wang, "Nanomotor lithography," *Nature Communications*, vol. 5, no. 1, 2014.

[5] S. Ghosh and A. Ghosh, "Mobile nanotweezers for active colloidal manipulation," *Science Robotics*, vol. 3, no. 14, article eaaq0076, 2018.

[6] W. Gao and J. Wang, "The environmental impact of micro/nanomachines. A review," *ACS Nano*, vol. 8, no. 4, pp. 3170–3180, 2014.

[7] F. Mou, D. Pan, C. Chen, Y. Gao, L. Xu, and J. Guan, "Magnetically modulated pot-like $MnFe_2O_4$ micromotors: nanoparticle assembly fabrication and their capability for direct oil removal," *Advanced Functional Materials*, vol. 25, no. 39, pp. 6173–6181, 2015.

[8] D. Vilela, J. Parmar, Y. Zeng, Y. Zhao, and S. Sanchez, "Graphene-based microbots for toxic heavy metal removal and recovery from water," *Nano Letters*, vol. 16, no. 4, pp. 2860–2866, 2016.

[9] R. Maria-Hormigos, M. Pacheco, B. Jurado-Sánchez, and A. Escarpa, "Carbon nanotubes-ferrite-manganese dioxide micromotors for advanced oxidation processes in water treatment," *Environmental Science: Nano*, vol. 5, no. 12, pp. 2993–3003, 2018.

[10] Q. Zhang, R. Dong, Y. Wu, W. Gao, Z. He, and B. Ren, "Light-driven Au-WO_3@C Janus micromotors for rapid photodegradation of dye pollutants," *ACS Applied Materials & Interfaces*, vol. 9, no. 5, pp. 4674–4683, 2017.

[11] J. Wang, R. Dong, Q. Yang et al., "One body, two hands: photocatalytic function- and Fenton effect-integrated light-driven micromotors for pollutant degradation," *Nanoscale*, vol. 11, no. 35, pp. 16592–16598, 2019.

[12] S. Wang, X. Liu, Y. Wang et al., "Biocompatibility of artificial micro/nanomotors for use in biomedicine," *Nanoscale*, vol. 11, no. 30, pp. 14099–14112, 2019.

[13] M. Luo, Y. Feng, T. Wang, and J. Guan, "Micro-/Nanorobots at Work in Active Drug Delivery," *Advanced Functional Materials*, vol. 28, no. 25, article 1706100, 2018.

[14] C. Nerbrand, L. Agreus, R. A. Lenner, P. Nyberg, and K. Svardsudd, "The influence of calcium and magnesium in drinking water and diet on cardiovascular risk factors in individuals living in hard and soft water areas with differences in cardiovascular mortality," *BMC Public Health*, vol. 3, 2003.

[15] J. Durlach, M. Bara, and A. Guiet-Bara, "Magnesium level in drinking water and cardiovascular risk factor: a hypothesis," *Magnesium*, vol. 4, no. 1, pp. 5–15, 1985.

[16] L. Kong, C. Chen, F. Mou et al., "Magnesium particles coated with mesoporous nanoshells as sustainable therapeutic-hydrogen suppliers to scavenge continuously generated hydroxyl radicals in long term," *Particle & Particle Systems Characterization*, vol. 36, no. 2, article 1800424, 2019.

[17] F. Mou, C. Chen, H. Ma, Y. Yin, Q. Wu, and J. Guan, "Self-propelled micromotors driven by the magnesium-water reaction and their hemolytic properties," *Angewandte Chemie International Edition*, vol. 52, no. 28, pp. 7208–7212, 2013.

[18] B. E.-F. de Ávila, P. Angsantikul, J. Li et al., "Micromotor-enabled active drug delivery for in vivo treatment of stomach infection," *Nature Communications*, vol. 8, no. 272, 2017.

[19] E. Karshalev, Y. Zhang, B. Esteban-Fernández de Ávila et al., "Micromotors for active delivery of minerals toward the treatment of iron deficiency anemia," *Nano Letters*, vol. 19, no. 11, pp. 7816–7826, 2019.

[20] L. Kong, N. F. Rosli, H. L. Chia, J. Guan, and M. Pumera, "Self-propelled autonomous Mg/Pt Janus micromotor interaction with human cells," *Bulletin of the Chemical Society of Japan*, vol. 92, no. 10, pp. 1754–1758, 2019.

[21] Z. Wu, L. Li, Y. Yang et al., "A microrobotic system guided by photoacoustic computed tomography for targeted navigation in intestines in vivo," *Science Robotics*, vol. 4, no. 32, article eaax0613, 2019.

[22] J. Li, S. Thamphiwatana, W. Liu et al., "Enteric micromotor can selectively position and spontaneously propel in the gastrointestinal tract," *ACS Nano*, vol. 10, no. 10, pp. 9536–9542, 2016.

[23] C. Chen, E. Karshalev, J. Guan, and J. Wang, "Magnesium-based micromotors: water-powered propulsion, multifunctionality, and biomedical and environmental applications," *Small*, vol. 14, no. 23, article 1704252, 2018.

[24] C. Chen, E. Karshalev, J. Li et al., "Transient micromotors that disappear when no longer needed," *ACS Nano*, vol. 10, no. 11, pp. 10389–10396, 2016.

[25] X. Wei, M. Beltrán-Gastélum, E. Karshalev et al., "Biomimetic micromotor enables active delivery of antigens for oral vaccination," *Nano Letters*, vol. 19, no. 3, pp. 1914–1921, 2019.

[26] D. Zhang, D. Wang, J. Li et al., "One-step synthesis of PCL/Mg Janus micromotor for precious metal ion sensing, removal and recycling," *Journal of Materials Science*, vol. 54, no. 9, pp. 7322–7332, 2019.

[27] F. Zhang, R. Mundaca-Uribe, H. Gong et al., "A macrophage-magnesium hybrid biomotor: fabrication and characterization," *Advanced Materials*, vol. 31, no. 27, article 1901828, 2019.

[28] L. Kong, N. Rohaizad, M. Z. M. Nasir, J. Guan, and M. Pumera, "Micromotor-assisted human serum glucose biosensing," *Analytical Chemistry*, vol. 91, no. 9, pp. 5660–5666, 2019.

[29] F. Mou, C. Chen, Q. Zhong, Y. Yin, H. Ma, and J. Guan, "Autonomous motion and temperature-controlled drug delivery of Mg/Pt-poly(*N*-isopropylacrylamide) Janus micromotors driven by simulated body fluid and blood plasma," *ACS Applied Materials & Interfaces*, vol. 6, no. 12, pp. 9897–9903, 2014.

[30] W. Haynes, *CRC Handbook of Chemistry and Physics*, CRC press, 2011.

[31] R. Pelton, "Temperature-sensitive aqueous microgels," *Advances in Colloid and Interface Science*, vol. 85, no. 1, pp. 1–33, 2000.

[32] J. Simmchen, V. Magdanz, S. Sanchez et al., "Effect of surfactants on the performance of tubular and spherical micromotors - a comparative study," *RSC Advances*, vol. 4, no. 39, pp. 20334–20340, 2014.

[33] L. Liu, T. Bai, Q. Chi et al., "How to make a fast, efficient bubble-driven micromotor: a mechanical view," *Micromachines*, vol. 8, no. 9, 2017.

[34] T. E. de Oliveira, D. Mukherji, K. Kremer, and P. A. Netz, "Effects of stereochemistry and copolymerization on the LCST of PNIPAM," *The Journal of Chemical Physics*, vol. 146, no. 3, article 034904, 2017.

[35] W. Zheng, N. An, J. Yang, J. Zhou, and Y. Chen, "Tough Al-alginate/Poly(*N*-isopropylacrylamide) Hydrogel with Tunable LCST for Soft Robotics," *ACS Applied Materials & Interfaces*, vol. 7, no. 3, pp. 1758–1764, 2015.

[36] Y. Tu, F. Peng, A. A. M. André, Y. Men, M. Srinivas, and D. A. Wilson, "Biodegradable hybrid stomatocyte nanomotors for drug delivery," *ACS Nano*, vol. 11, no. 2, pp. 1957–1963, 2017.

[37] B.-E. Pinchasik, H. Möhwald, and A. G. Skirtach, "Mimicking bubble use in nature: propulsion of janus particles due to hydrophobic-hydrophilic interactions," *Small*, vol. 10, no. 13, pp. 2670–2677, 2014.

[38] H. Wang, G. Zhao, and M. Pumera, "Crucial role of surfactants in bubble-propelled microengines," *The Journal of Physical Chemistry C*, vol. 118, no. 10, pp. 5268–5274, 2014.

[39] G. Lee and J. Park, "Reaction of zero-valent magnesium with water: potential applications in environmental remediation," *Geochimica et Cosmochimica Acta*, vol. 102, pp. 162–174, 2013.

[40] T. A. Vetter and D. Philip Colombo Jr., "Kinetics of platinum-catalyzed decomposition of hydrogen peroxide," *Journal of Chemical Education*, vol. 80, no. 7, pp. 788-789, 2003.

[41] M. B. Rubin and R. M. Noyes, "Chemical oscillations and instabilities. 77. Measurements of critical supersaturation for homogeneous nucleation of bubbles," *The Journal of Physical Chemistry*, vol. 91, no. 15, pp. 4193–4198, 1987.

[42] Q. Chen, L. Luo, H. Faraji, S. Feldberg, and H. White, "Electrochemical measurements of single H_2 Nanobubble nucleation and stability at Pt nanoelectrodes," *The Journal of Physical Chemistry Letters*, vol. 5, no. 20, pp. 3539–3544, 2014.

[43] A. S. Vikulina, S. T. Aleed, T. Paulraj et al., "Temperature-induced molecular transport through polymer multilayers coated with PNIPAM microgels," *Physical Chemistry Chemical Physics*, vol. 17, no. 19, pp. 12771–12777, 2015.

[44] J. Wahrmund, J.-W. Kim, L.-Y. Chu et al., "Swelling kinetics of a microgel shell," *Macromolecules*, vol. 42, no. 23, pp. 9357–9365, 2009.

[45] T. Tanaka, E. Sato, Y. Hirokawa, S. Hirotsu, and J. Peetermans, "Critical kinetics of volume phase transition of gels," *Physical Review Letters*, vol. 55, no. 22, pp. 2455–2458, 1985.

[46] M. Huang, J. Schofield, P. Gaspard, and R. Kapral, "From single particle motion to collective dynamics in Janus motor systems," *Journal of Chemical Physics*, vol. 150, no. 12, article 124110, 2019.

[47] Z. Liu, Y. Zhu, J. R. Clausen, J. B. Lechman, R. R. Rao, and C. K. Aidun, "Multiscale method based on coupled lattice-Boltzmann and Langevin-dynamics for direct simulation of nanoscale particle/polymer suspensions in complex flows," *International Journal for Numerical Methods in Fluids*, vol. 91, no. 5, pp. 228–246, 2019.

[48] S. Nakata, Y. Iguchi, S. Ose, M. Kuboyama, T. Ishii, and K. Yoshikawa, "Self-rotation of a camphor scraping on water: new insight into the old problem," *Langmuir*, vol. 13, no. 16, pp. 4454–4458, 1997.

[49] A. Einstein, "Über die von der molekularkinetischen Theorie der Wärme geforderte Bewegung von in ruhenden Flüssigkeiten suspendierten Teilchen," *Annalen der Physik*, vol. 322, no. 8, pp. 549–560, 1905.

[50] J. R. Howse, R. A. L. Jones, A. J. Ryan, T. Gough, R. Vafabakhsh, and R. Golestanian, "Self-motile colloidal particles: from directed propulsion to random walk," *Physical Review Letters*, vol. 99, no. 4, article 048102, 2007.

[51] W. Yang, J. Li, Z. Xu, J. Yang, Y. Liu, and L. Liu, "A Eu-MOF/EDTA-NiAl-CLDH fluorescent micromotor for sensing and removal of Fe^{3+} from water," *Journal of Materials Chemistry C*, vol. 7, no. 33, pp. 10297–10308, 2019.

[52] L. Wang, H. Zhu, Y. Shi et al., "Novel catalytic micromotor of porous zeolitic imidazolate framework-67 for precise drug delivery," *Nanoscale*, vol. 10, no. 24, pp. 11384–11391, 2018.

[53] J. A. M. Delezuk, D. Ramirez-Herrera, B. Esteban-Fernández de Ávila, and J. Wang, "Chitosan-based water-propelled micromotors with strong antibacterial activity," *Nanoscale*, vol. 9, no. 6, pp. 2195–2200, 2017.

[54] K. Mahesh, R. Balaji, and K. Dhathathreyan, "Studies on noble metal-free carbon-based cathodes for magnesium-hydrogen peroxide fuel cells," *Ionics*, vol. 21, no. 9, pp. 2603–2607, 2015.

[55] J. Li, G. Huang, M. Ye, M. Li, R. Liu, and Y. Mei, "Dynamics of catalytic tubular microjet engines: dependence on geometry and chemical environment," *Nanoscale*, vol. 3, no. 12, pp. 5083–5089, 2011.

[56] B. Khezri, S. M. B. Mousavi, L. Krejčová, Z. Heger, Z. Sofer, and M. Pumera, "Ultrafast electrochemical trigger drug delivery mechanism for nanographene micromachines," *Advanced Functional Materials*, vol. 29, no. 4, article 1806696, 2019.

[57] J. Hwang, H.-M. Yang, K.-W. Lee, Y.-I. Jung, K. J. Lee, and C. W. Park, "A remotely steerable Janus micromotor adsorbent for the active remediation of Cs-contaminated water," *Journal of Hazardous Materials*, vol. 369, pp. 416–422, 2019.

[58] H. Zhu, S. Nawar, J. Werner et al., "Hydrogel micromotors with catalyst-containing liquid core and shell," *Journal of Physics: Condensed Matter*, vol. 31, no. 21, article 214004, 2019.

[59] E. Matsuo and T. Tanaka, "Kinetics of discontinuous volume-phase transition of gels," *The Journal of Chemical Physics*, vol. 89, no. 3, pp. 1695–1703, 1988.

[60] R. Millington, "Permeability of Porous Media," *Nature*, vol. 183, no. 4658, pp. 387-388, 1959.